PCCP

PAPER

View Article Online
View Journal | View Issue

Cite this: *Phys. Chem. Chem. Phys.*, 2017, **19**, 6546

Interfacial electronic structures revealed at the rubrene/$CH_3NH_3PbI_3$ interface

Gengwu Ji,†[ab] Guanhaojie Zheng,†[ab] Bin Zhao,[a] Fei Song,[a] Xiaonan Zhang,[ab] Kongchao Shen,[a] Yingguo Yang,[a] Yimin Xiong,[c] Xingyu Gao,*[a] Liang Cao*[c] and Dong-Chen Qi*[d]

Received 7th November 2016,
Accepted 31st January 2017

DOI: 10.1039/c6cp07592d

rsc.li/pccp

The electronic structures of rubrene films deposited on $CH_3NH_3PbI_3$ perovskite have been investigated using *in situ* ultraviolet photoelectron spectroscopy (UPS) and X-ray photoelectron spectroscopy (XPS). It was found that rubrene molecules interacted weakly with the perovskite substrate. Due to charge redistribution at their interface, a downward 'band bending'-like energy shift of ~0.3 eV and an upward band bending of ~0.1 eV were identified at the upper rubrene side and the $CH_3NH_3PbI_3$ substrate side, respectively. After the energy level alignment was established at the rubrene/$CH_3NH_3PbI_3$ interface, its highest occupied molecular orbital (HOMO)–valence band maximum (VBM) offset was found to be as low as ~0.1 eV favoring the hole extraction with its lowest unoccupied molecular orbital (LUMO)–conduction band minimum (CBM) offset as large as ~1.4 eV effectively blocking the undesired electron transfer from perovskite to rubrene. As a demonstration, simple inverted planar solar cell devices incorporating rubrene and rubrene/poly(3,4-ethylenedioxythiophene):poly(styrenesulfonate) (PEDOT:PSS) hole transport layers (HTLs) were fabricated in this work and yielded a champion power conversion efficiency of 8.76% and 13.52%, respectively. Thus, the present work suggests that a rubrene thin film could serve as a promising hole transport layer for efficient perovskite-based solar cells.

Introduction

In recent years, organic–metal halide perovskite solar cells (PSCs) have attracted widespread interest due to their solution processability, low cost, and extraordinary power conversion efficiency (PCE) of over 20%.[1–3] In PSCs, $APbX_3$ (A = methylammonium (MA), formamidinium (FA); X = Br, Cl and I) perovskite materials serve as both active light absorbers and charge carrier transporters. Their high PCE is mainly ascribed to the outstanding optoelectronic properties of perovskite, such as appropriate bandgap, long hole–electron diffusion length,[4,5] low trap-state density and long carrier diffusion in organolead trihalide perovskite single crystals,[6] excellent charge carrier mobility,[7] and high absorption coefficient.[8] The quantum leap in the PCE of PSCs from 3.8% to 21.1% within just five years is mainly attributed to the fine-tuning of the perovskite composition and fabrication techniques.

In a regular PSC, the perovskite active layer is normally sandwiched between a scaffold layer of TiO_2, Al_2O_3 or ZrO_2, and a hole transport layer (HTL). Two of the most important processes determining device performances including PCE, open-circuit voltage (V_{oc}), and stability are the charge carrier extraction and exciton dissociation at the perovskite/electrode interfaces, which can be engineered by optimizing the interfacial electronic structures (energy level alignment)[9] to enhance the selective charge carrier collection efficiency. For instance, organic semiconductors such as the polytriarylamine (PTAA) polymer[10] and the hole acceptor 2,2′,7,7′-tetrakis(*N*,*N*-di-*p*-methoxyphenylamine)-9,9′-spirobifuorene (Spiro-OMeTAD)[11,12] introduced between anode and perovskite increase PCE significantly, demonstrating an effective route to improving device performance *via* interfacial engineering. It is well-known that an unfavorable interfacial energy level mismatch, *i.e.* the valence band (VB) of perovskite lies above the highest occupied molecular orbital (HOMO) of organic HTLs with a large offset, will reduce the carrier transport efficiency. Therefore, it is important to investigate the interfacial electronic structures of potential HTLs on perovskite in the search of suitable candidates as efficient HTLs in PSCs.[13–15] It will not only provide fundamental insight into relevant interfacial electronic processes, but also serve as an important guide for the rational design and engineering of PSCs.

[a] *Shanghai Institute of Applied Physics, Chinese Academy of Sciences, 2019 Jia Luo Road, Shanghai, 201800, P. R. China. E-mail: gaoxingyu@sinap.ac.cn*
[b] *University of Chinese Academy of Sciences, 19A Yuquan Road, Beijing, 100049, China*
[c] *High Magnetic Field Laboratory, Chinese Academy of Sciences, 350 Shushanhu Road, Hefei, 230031, Anhui, P. R. China. E-mail: lcao@hmfl.ac.cn*
[d] *Department of Chemistry and Physics, La Trobe Institute for Molecular Science, La Trobe University, Melbourne, Victoria 3086, Australia. E-mail: D.Qi@latrobe.edu.au*
† These authors contributed equally.

There are two essential criteria for an ideal HTL: high hole mobility and matched energy levels at the HTL/perovskite interface.[16,17] A number of materials have been adopted as HTLs including small molecules (such as Spiro-MeOTAD,[11] *N*,*N*,*N*′,*N*′-tetraphenyl-benzidine (TPB) derivatives,[18] and 6,13-bis(triisopropylsilylethynyl) pentacence (TIPS-pentacence)),[19] polymers (such as poly(3,4-ethylenedioxythiophene):poly(styrenesulfonate) (PEDOT:PSS),[20] poly(3-hexylthiophene) (P3HT),[21] poly[[2,5-bis(2-octyldodecyl)-2,3,5,6-tetrahydro-3,6-dioxopyrrolo[3,4-*c*]pyrrole-1,4-diyl]-alt–[[2,2′-(2,5-thiophene)bis-thieno[3,2-*b*]thiophen]-5,5′-diyl]] (a DPP-based polymer),[22] and PTAA[10]) and metal oxides (such as NiO).[23] Among them, Spiro-OMeTAD has been most intensively studied because PSCs incorporated with a Spiro-OMeTAD HTL have achieved the world-record highest PCE up to 21.1%.[3] This remarkable achievement is largely attributed to a matched energy level alignment at the Spiro-OMeTAD/perovskite interface which minimizes energy loss due to electron–hole recombination by facilitating efficient hole extraction and effectively blocking electron conduction.[16,17] However, the complicated synthesis and purification processes of Spiro-OMeTAD obviously hinder its practical application.[24] In addition, devices based on Spiro-OMeTAD also suffer from instability caused by the oxidization of dopants/additives in spiro-OMeTAD.[25] Therefore, it is important to seek a more stable and economically viable HTL material to promote effective exciton dissociation/charge extraction.[19]

Rubrene with a molecular structure shown in Fig. 1 is a model organic semiconducting molecule with high hole mobility and impressive chemical stability.[26,27] It has been widely used in organic light emitting diodes (OLEDs),[28] organic field effect transistors (OFETs),[29] organic solar concentrators (OSCs),[26] and organic photovoltaics (OPVs).[30] In addition, rubrene has an ionization energy (IE) of ~5.3 eV,[31] which is slightly smaller than that of 5.7–6.4 eV for iodide based perovskite, and a relatively low electron affinity (EA).[32] This suggests that rubrene could be a suitable hole transport material for PSCs. However, it is well-known that energy level alignments derived from the respective bulk electronic properties of the constituent compounds at organic/inorganic heterojunctions by assuming vacuum level alignment (Schottky–Mott limit) are often not reliable due to the presence of interfacial dipoles.[33–37] Therefore, experimental characterization of the electronic structures at the rubrene/perovskite interface is inevitable for the establishment of interfacial energetics.

The present work aims to explore the potential use of rubrene molecules in PSCs as a HTL by investigating the rubrene/perovskite interfacial electronic structures. Perovskite films with a (110) surface orientation, which is expected to favor hole injection,[38] are studied by synchrotron-based grazing incident X-ray diffraction (GIXRD). The electronic structures at the rubrene/polycrystalline $CH_3NH_3PbI_3$ interface are investigated using *in situ* ultraviolet photoemission spectroscopy (UPS) and X-ray photoemission spectroscopy (XPS). It was found that rubrene molecules interacted weakly with $CH_3NH_3PbI_3$. Due to charge redistribution at their interface, a downward 'band bending'-like energy shift of ~0.3 eV and an upward band bending of ~0.1 eV were identified at the rubrene thin film side and the $CH_3NH_3PbI_3$ substrate side, respectively. Moreover, a rather low highest occupied molecular orbital (HOMO)–valence band maximum (VBM) offset of 0.1–0.4 eV was found at their interface favoring hole transfer from $CH_3NH_3PbI_3$ to rubrene, whereas there was a large lowest unoccupied molecular orbital (LUMO)–conduction band minimum (CBM) offset efficiently blocking electron transfer from perovskite to rubrene at the interface. Eventually, the rubrene/perovskite based inverted planar PSCs fabricated employing a simple device architecture of Ag/phenyl-C_{61}-butyric acid methyl ester (PCBM)/$CH_3NH_3PbI_3$/rubrene/ITO and Ag/PCBM/$CH_3NH_3PbI_3$/Rubrene/PEDOT:PSS/ITO were found to yield a PCE of 8.76% and 13.52%, respectively.

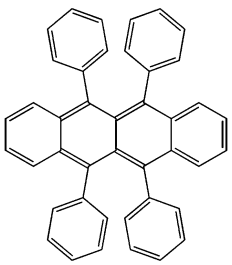

Fig. 1 Molecular structure of a rubrene molecule.

Results and discussion

Microstructure and surface morphology

It is well-known that the microstructure and morphology of perovskite films, which strongly depend on the preparation conditions of the films,[39,40] play critical roles in determining the performance of solar cell devices. The structure and morphology of perovskite films, which depend sensitively on film stoichiometry, have significant influences on the electronic structures of perovskite thin films and thus their device performances.[41] In particular, their IE and density of states close to the VB[32] change with their stoichiometry tuned by (i) varying the mixing ratios of PbI_2 and CH_3NH_3I precursors for perovskite formation, (ii) changing the post-treatment process,[42–44] (iii) mixing cations such as $CH(NH_2)_2^+$,[45] $CHNH_3^+$,[46] and Sn^{2+},[47] or (iv) substituting halides.[48] It has been found that $CH_3NH_3PbI_3$ films with a molar ratio around 1 : 1 (also adopted in the present study) show a preferential in-plane orientation of the (110) plane with the highest density of states close to the VB (serving as the gauge of the transport properties of the perovskite films), which leads to the highest PCE[32] and the maximum J_{sc}[49] among the resulting devices.

In the following sections, GIXRD and scanning electron microscopy (SEM) were used to investigate the microstructure and morphology of the as-prepared film. Fig. 2a and b report the 2D GIXRD pattern and SEM image of the as-prepared $CH_3NH_3PbI_3$ film, respectively. In Fig. 2a, the bright rings at q_r = 10.0, 14.2, 17.0, 20.0, and 22.0 nm^{-1} correspond to the (110), (200), (202), (220) and (310) planes of $CH_3NH_3PbI_3$ perovskite crystals, respectively, evidencing the formation of a high-quality polycrystalline perovskite film.[50] Moreover, the brightest spot at q_z = 10 nm^{-1}

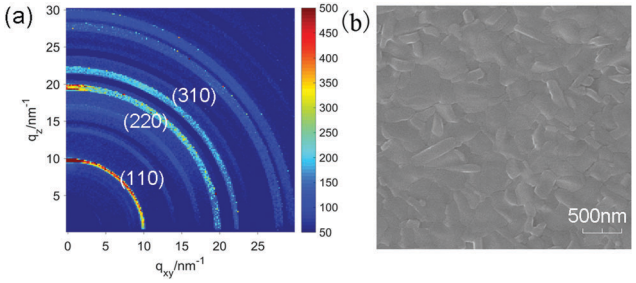

Fig. 2 (a) GIXRD pattern and (b) SEM image of the perovskite $CH_3NH_3PbI_3$ film.

proves that the perovskite (110) plane has a strong preferential out-of-plane orientation. The absence of additional diffraction rings at $\sim 9\ nm^{-1}$ and $\sim 7\ nm^{-1}$ originating from spurious PbI_2 phases formed due to desorption of CH_3NH_3I species after air exposure further confirms the quality of the film.[51] From Fig. 2b, it is clear that the as-prepared perovskite film exhibits a flat, uniform, pin-hole free surface morphology with densely packed grains of 0.2 to 0.5 μm in size. All these observations show that the quality of the perovskite thin film prepared in the present study is similar to those reported in solar cell devices.[38,52]

Interfacial reaction and electronic structure

UPS and XPS were performed to investigate the electronic structures and possible chemical interaction at the rubrene/$CH_3NH_3PbI_3$ interface. Fig. 3 shows the evolution of the secondary electron cutoff (SECO) and VB spectra with increasing rubrene thickness on $CH_3NH_3PbI_3$. The work function (WF) of the pristine perovskite $CH_3NH_3PbI_3$ thin film, as indicated by the SECO energy position, is found to be $\sim$4.4 eV, consistent with a previous report.[17,53] Upon the deposition of 3 Å rubrene molecules, the WF undergoes a slight decrease to a value of $\sim$4.2 eV and remains almost constant even at the maximum rubrene thickness of 108 Å, indicating the presence of a small interface dipole.

The VB spectra as a function of rubrene thickness are displayed in Fig. 3b. The VBM of $CH_3NH_3PbI_3$ occurs at $\sim$1.4 eV (indicated by an arrow) below the Fermi level (E_F), agreeing well with the results reported previously.[17,54] The spectral feature at $\sim$1.4 eV, which becomes visible just upon the deposition of 6 Å rubrene molecules, is attributed to the HOMO of rubrene molecules. At a thickness of 24 Å, the molecular frontier orbitals of rubrene molecules[55] become dominant in the VB spectra. No additional VB features are observed in the interfacial regime between 3 and 24 Å, implying weak rubrene–$CH_3NH_3PbI_3$ interaction. It is evident that the HOMO position shifts to lower binding energy with the increase of rubrene thickness. Fig. 3c shows the close up of VB features after subtracting the perovskite substrate signal, taking the attenuation of the substrate signal into consideration. The HOMO onset, which is located at $\sim$1.2 eV at 3 Å thickness, gradually shifts to lower binding energy and saturate at $\sim$0.9 eV at 36 Å.

The core-level spectra serve as an additional tool to investigate the chemical interaction and possible 'band bending' at the rubrene/$CH_3NH_3PbI_3$ interface. Fig. 4 shows the evolution of the C 1s spectrum. The C 1s core-level of the pristine $CH_3NH_3PbI_3$ substrate contains two peaks. The main peak located at $\sim$286.6 eV is attributed to methyl carbon-atoms, and the lower binding energy peak at $\sim$285.2 eV is assigned to contamination.[16] The dominant peak of the substrate decreases in intensity with increasing rubrene thickness. A new feature labeled as C_R, which originates from rubrene molecules,[55] gradually develops and overlaps with the shoulder peak of pristine $CH_3NH_3PbI_3$. After deconvolution, the binding energy of the C_R peak is found to shift to lower binding energy by as much as $\sim$0.4 eV and saturates at 36 Å, which agrees well with the HOMO onset shift of $\sim$0.3 eV, revealing the common origin of the 'band bending'-like effect. In addition, no new feature is observed, ruling out strong chemical molecule–substrate interactions.

Fig. 5 displays the evolution of the Pb $4f_{7/2}$ and I $3d_{5/2}$ core-level spectra of the $CH_3NH_3PbI_3$ substrate upon the deposition of rubrene molecules. Again, no new features are visible through the whole deposition, excluding any possible strong rubrene–$CH_3NH_3PbI_3$ interactions. The binding energies of I $3d_{5/2}$ and

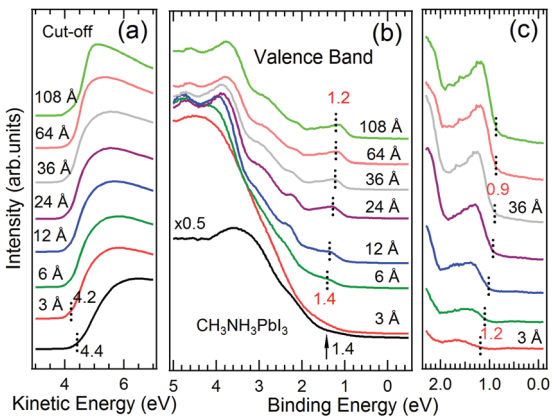

Fig. 3 (a) Low kinetic energy SECO, (b) VB spectra, and (c) the close-up of VB features after subtracting the substrate signal for rubrene on $CH_3NH_3PbI_3$ with increasing thickness.

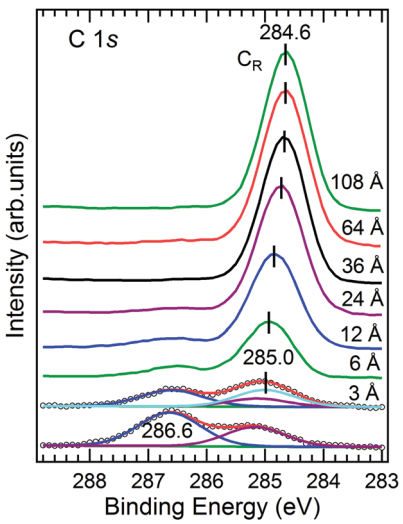

Fig. 4 The evolution of the C 1s core-level spectra of rubrene molecules on $CH_3NH_3PbI_3$. All spectra were fitted using Shirley plus linear background.

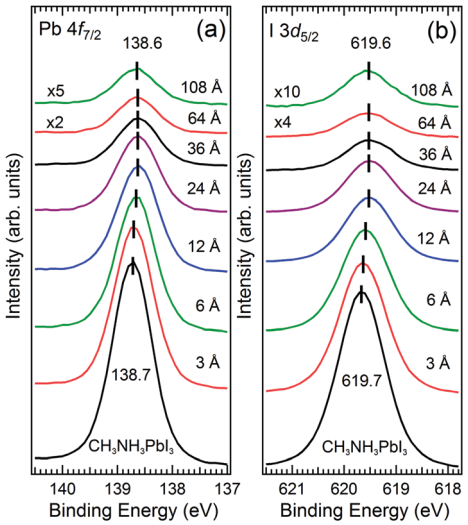

Fig. 5 (a) Pb $4f_{7/2}$ and (b) I $3d_{5/2}$ core-level spectra as a function of the rubrene thickness.

Pb $4f_{7/2}$ for the pristine film are located at ~138.7 eV, and ~619.7 eV, respectively, consistent with the values reported in the literature of $CH_3NH_3PbI_3$.[56] Furthermore, all of their binding energies shift in the same fashion to lower binding energy monotonically by ~0.1 eV after rubrene deposition, indicating the presence of interfacial charge redistribution at the rubrene/$CH_3NH_3PbI_3$ interface.

Energy level alignment

On the basis of the UPS and XPS results, the schematic energy level alignment at the rubrene/$CH_3NH_3PbI_3$ interface can be depicted in Fig. 6. The VBM of $CH_3NH_3PbI_3$ is found at ~1.4 eV below the Fermi level with its conduction band minimum (CBM) placed ~0.2 eV above the Fermi level considering a band gap of 1.6 eV.[57,58] This is consistent with the intrinsic n-type nature of $CH_3NH_3PbI_3$ produced by a 1 : 1 precursor ratio.[41] In addition, post-annealing further pushed up the Fermi level towards the conduction band possibly due to the presence of I vacancies on the surface caused by the evaporation of CH_3NH_3I from the surface of the perovskite film, resulting in a heavily n-doped film.[41] The WF of $CH_3NH_3PbI_3$ is ~4.4 eV, consistent with the value reported previously.[17] The IE and EA of rubrene molecules are calculated to be 5.1 ± 0.1 eV and 2.2 ± 0.1 eV (assuming a transport band gap of 2.9 eV[59,60]), respectively. An upward 'band bending'-like shift of ~0.1 eV at the $CH_3NH_3PbI_3$ substrate and a downward 'band bending'-like shift of ~0.3 eV in the molecular layer are established at the interface, respectively. Consequently, considering the weak molecule–substrate interaction, the 'band bending'-like effect is due to the presence of interfacial charge transfer: *i.e.* electron transfer from the $CH_3NH_3PbI_3$ substrate to the rubrene layer to establish thermodynamic equilibrium.[33,61] The electrostatic field associated with the 'band bending'-like effect at the rubrene/$CH_3NH_3PbI_3$ interface could potentially facilitate the hole carrier collection from $CH_3NH_3PbI_3$ to rubrene. The energy level offset (ΔE_v), as indicated by the difference between rubrene HOMO onset and $CH_3NH_3PbI_3$ VBM, ranges from 0.1 eV to 0.4 eV depending on the rubrene thickness, which is comparable with that of 0.4 eV at the Spiro-OMeTAD/$CH_3NH_3PbI_3$ interface.[17] The electron blocking barrier (ΔE_c) as indicated by the distance between rubrene LUMO and $CH_3NH_3PbI_3$ CBM was estimated to be 1.4–1.7 eV. The small ΔE_v and large electron blocking barrier of ΔE_c are expected to facilitate hole extraction and reduce charge recombination and thus may lead to larger V_{oc} and higher short-circuit current (J_{sc}) in $CH_3NH_3PbI_3$ perovskite based solar cells.[16,17] In addition, a smaller ΔE_v will lead to a lower built-in field and smaller thermionic losses in the process of hole extraction.[17] Coupled with the larger carrier mobility in rubrene compared to that in Spiro-OMeTAD, rubrene molecules are likely to be a suitable HTL candidate replacing Spiro-OMeTAD in PSCs.

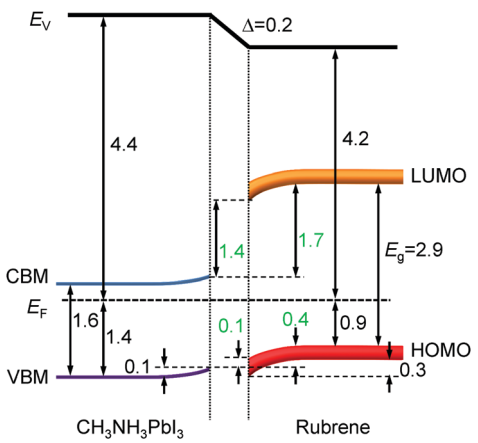

Fig. 6 The energy level diagram at the rubrene/$CH_3NH_3PbI_3$ interface (units: eV).

Performance of solar cell devices

To test the device performance of PSCs incorporating rubrene as the HTL, we fabricated inverted planar PSCs with a architecture of Ag/PCBM/$CH_3NH_3PbI_3$/rubrene/ITO and compared with that of inverted planar Ag/PCBM/$CH_3NH_3PbI_3$/PEDOT:PSS/ITO devices. We employed the inverted device structure because the annealing process at 150 °C following spin-coating of rubrene thin films is detrimental to the performance and stability of perovskite thin films. PEDOT:PSS has been selected as the benchmark reference because it is commonly used as a HTL in inverted planar PSCs with good performance.[62] Fig. 7a compares the current density–voltage (J–V) characteristics of these two solar cell devices measured in both the forward and reverse scanning directions with their corresponding device parameters summarized in Table 1. The PEDOT:PSS-based device without systematic optimization yielded a 11.16% PCE with a V_{oc} of 0.85 V, a J_{sc} of 17.80 mA cm^{-2}, and a fill factor (FF) of 0.72 for the reverse scan in the best case, whereas the highest reported PCE can reach 18.1%.[62] Under similar experimental conditions, the rubrene-based champion device here achieved a PCE of 8.76% with a V_{oc} of 0.85 V, a J_{sc} of 16.84 mA cm^{-2}, and a FF of 0.61 in the reverse scan direction. As expected, PEDOT:PSS-based device shows reduced J–V hysteresis because of better balanced electron flux and hole

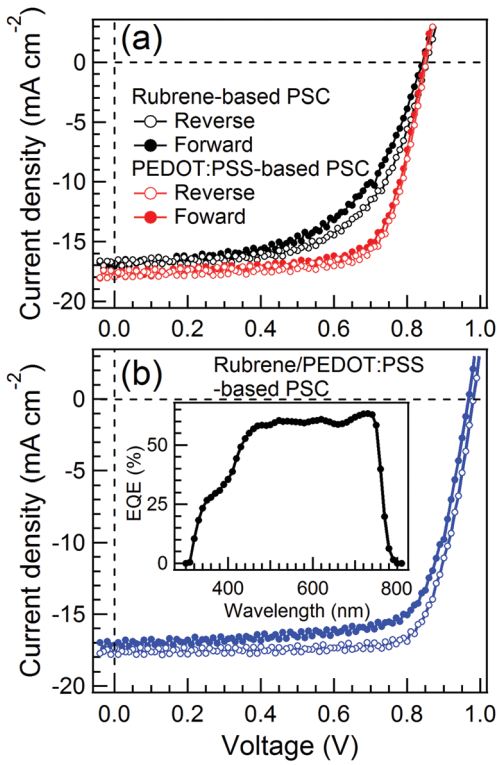

Fig. 7 (a) *J–V* curves for the champion Ag/PCBM/$CH_3NH_3PbI_3$/rubrene/ITO and Ag/PCBM/$CH_3NH_3PbI_3$/PEDOT:PSS/ITO solar cell devices measured in both the forward (−2.0 to 1.2 V) and reverse (1.2 to −2.0 V) directions. (b) *J–V* curves of the champion Ag/PCBM/$CH_3NH_3PbI_3$/rubrene/PEDOT:PSS/ITO solar cell device measured in both the forward (solid circles) and reverse (open circles) scans. The inset shows the EQE spectrum of a representative rubrene/PEDOT:PSS-based PSC.

Table 1 Summary of device performance parameters of the perovskite solar cells with PEDOT:PSS, rubrene, or rubrene/PEDOT:PSS films as HTLs

HTL	Scan direction	V_{oc} (V)	J_{sc} (mA cm^{-2})	FF	PCE (%)	R_s (Ω cm^2)	R_{sh} (Ω cm^2)
PEDOT:PSS	Forward	0.85	17.71	0.72	10.75	5.67	54.05
	Reverse	0.85	17.80	0.72	11.16	5.90	58.82
Rubrene	Forward	0.84	17.08	0.56	7.90	8.89	43.47
	Reverse	0.85	16.84	0.61	8.76	8.69	66.15
Rubrene/	Forward	0.97	17.15	0.72	12.10	6.17	48.69
PEDOT:PSS	Reverse	0.98	17.36	0.79	13.52	6.04	72.09

flux as well as the reduced number of surface traps.[54] It is noticed that rubrene-based device exhibits undesired *J–V* hysteresis behavior. However, it is worth mentioning that a V_{oc} comparable to that of the PEDOT:PSS-based device is achieved, corroborating the optimal energy level alignment and efficient hole extraction at the rubrene/perovskite interface. In addition, the superior stability of rubrene can overcome the issues that both PEDOT:PSS[63] and Spiro-OMeTAD are suffering from. The relatively low current density and FF in the rubrene-based PSC device are possibly due to the poorer rubrene film quality prepared by spin-coating as compared to other film deposition techniques, such as vapor phase deposition. To further improve the film quality, we prepared rubrene films on top of PEDOT:PSS films to fabricate rubrene/PEDOT:PSS-based devices with the *J–V* curves of the champion device shown in Fig. 7b. The champion device yielded a relatively high PCE of 13.52% with a V_{oc} of 0.98 V, a J_{sc} of 17.36 mA cm^{-2}, and a FF of 0.79 in the reverse scan direction. To confirm the accuracy of the *J–V* measurements of the devices the corresponding external quantum efficiency (EQE) spectrum of a representative rubrene/PEDOT:PSS-based PSC was collected under illumination of monochromatic light as shown in the inset of Fig. 7b. A J_{sc} of 14.2 mA cm^{-2} calculated by integrating the EQE spectrum over the solar spectrum is close to the J_{sc} obtained from the *J–V* measurement. Our results also suggest much room for device optimization and performance improvement. For example, rubrene thin films deposited *via* organic molecular beam deposition would have a better morphology and crystallinity with much less charge-trapping grain boundaries than spin-coated films. Moreover, replacing the Ag electrode with other ones, such as Au, could yield higher PCE.

Experimental

The $CH_3NH_3PbI_3$ thin films were prepared *via* a one-step process as reported in the literature.[62] The perovskite precursor solution was prepared by dissolving PbI_2 (99%, Sigma-Aldrich) and CH_3NH_3I (99%, Shanghai MaterWin New Materials Co., Ltd) in 1 ml anhydrous *N*,*N*-dimethylformamide (DMF) in a molar ratio of 1 : 1. Subsequently, the as-prepared precursor solution was kept at 60 °C overnight. After cooling down to room temperature, 0.1 mL hydrogen iodide (HI) with a concentration of 100 μL mL was added into the solution and stirred for 30 min. The $CH_3NH_3PbI_3$ perovskite thin films were obtained by spin-coating the mixed precursor solution onto clean TiO_2 coated FTO (Zhuhai Kaivo Optoelectronic Technology Co., Ltd) at 3000 rpm for 30 s, and subsequently annealed at 100 °C for 20 min in a glove box under argon atmosphere.

The microstructures of the as-prepared perovskite films were investigated by GIXRD performed at the BL14B1 beamline of the Shanghai Synchrotron Radiation Facility (SSRF) using X-ray with a wavelength of 1.24 Å at a grazing incidence angle of 0.2°. The GIXRD patterns were collected by using a MarCCD 225 detector with a sample–detector distance of 160 mm, which will be presented later in q coordinates using the equation $q = 4\pi \sin\theta/\lambda$, where θ is half of the diffraction angle and the λ of 1.24 Å is the wavelength of X-rays with a photon energy of 10 keV. In the present GIXRD data, q has been calibrated by measuring the XRD of a lanthanum hexaboride reference sample. The SEM images of the films were taken by using a high resolution electron beam lithography system (CABL-9000C).

For photoemission experiments, the as-prepared perovskite films were transferred into an ultrahigh vacuum (UHV) system with a base pressure better than 2×10^{-10} mbar and kept in vacuum overnight for degassing at 100 °C. After being degassed, rubrene molecules (99.9%, Sigma-Aldrich) were deposited onto perovskite substrates using a standard Knudsen-cell. Photoemission measurements were performed *in situ* at room temperature after each deposition using a PHOIBOS 100 analyzer

together with a monochromatic X-ray source (Al Kα: 1486.61 eV) for XPS and a helium light lamp (He I: 21.2 eV) for UPS, respectively. Using a gold reference sample, the instrumental energy resolution for XPS and UPS was estimated to be 0.45 eV and 15 meV, respectively. The rubrene film thicknesses were calibrated by the attenuation of Pb $4f_{7/2}$ XPS intensities from the perovskite substrates after each deposition. To extract the WF from the SECO in the UPS spectra, a −10 V bias was applied to the samples. All photoemission spectra were collected at normal emission, and the binding energy was referred to the Fermi level of a sputter-cleaned gold foil electrically connected to the sample. The least-squares peak fit analysis of XPS spectra was performed by using the XPSpeak software.

Rubrene/perovskite based solar cells were fabricated by constructing the inverted planar device architecture of Ag/PCBM/$CH_3NH_3PbI_3$/rubrene/ITO.[64] Rubrene was dissolved in toluene at a concentration of 10 mg mL^{-1} and stirred overnight at room temperature. The rubrene solution was spin-coated on a plasma-cleaned and patterned ITO substrate at 1200 rpm for 60 s. After baking at 150 °C for 1 hour for the formation of rubrene thin films (~20 nm), the perovskite precursor solution (HI added) was spin-coated on the rubrene/ITO substrate and subsequently annealed at 100 °C for 2 min to form perovskite films (see ref. 62 and 65 for detailed information). The rubrene film thickness of ~20 nm was chosen according to ref. 65. After the formation of perovskite films (350 nm), PCBM (40 nm, 99%, Sigma) used as the electron transport layer was deposited by spin-coating the PCBM precursor solution (10 mg mL^{-1} dissolved in chlorobenzene) at 2000 rpm for 45 s. Finally, the films were transferred into a thermal evaporation chamber for Ag electrode (100 nm) deposition. The fabrication procedures were carried out in a nitrogen-filled glove box (<0.1 ppm O_2 and H_2O). For comparison, we fabricated inverted planar solar cell devices using PEDOT:PSS (Sigma) films as HTLs instead of rubrene thin films. We also fabricated devices by forming rubrene films (~20 nm) on top of PEDOT:PSS films to further improve the rubrene film quality prepared by spin-coating. The efficiency and *J–V* curves characteristics were measured under AM 1.5G illumination at 100 mW cm^{-2} using a Keithley 2400 sourcemeter. The EQE spectrum was measured by using a power source (150W Xenon lamp) with a monochromator (MonoRa-500i: DONGWOO OPTRON Co., Ltd) and a potentiostat (IviumStat: IVIU).

Conclusions

The electronic structures at the rubrene/perovskite $CH_3NH_3PbI_3$ interface have been studied by employing UPS and XPS. Rubrene molecules interacted weakly with the $CH_3NH_3PbI_3$ substrate. A downward 'band bending'-like energy shift of ~0.3 eV at the rubrene molecular layer and a ~0.1 eV upward 'band bending' at the $CH_3NH_3PbI_3$ substrate layer were identified due to the charge exchange at interface. The HOMO–VBM offset ΔE_v and LUMO–CBM offset ΔE_c at the rubrene/perovskite $CH_3NH_3PbI_3$ interface were found to be ~0.1 eV and ~1.4 eV, respectively. This optimal energy level alignment can potentially facilitate hole extraction from $CH_3NH_3PbI_3$ to the rubrene HTL and effectively block electron transfer from perovskite to rubrene. Our spectroscopic results suggest that rubrene can serve as a suitable hole transport material in PSCs.

Planar PSCs without a (mesoporous) scaffold layer have attracted considerable attention due to the simplification of the device fabrication process and compatibility with flexible substrates.[64,66] In addition, perovskite sandwiched between two organic charge transport layers shows a higher PCE of more than 18%,[62] evidencing the promising application of organic semiconductors in planar perovskite based electronic devices. The present inverted PSCs based on rubrene and rubrene/PEDOT:PSS HTLs achieve a champion PCE of 8.76% and 13.52%, respectively. In comparison with PEDOT:PSS-based devices, their comparable or even higher PCE prove that rubrene is a promising HTL material for PSCs. Our study therefore not only demonstrates that rubrene can be an effective HTL for PSCs, but also provides insights into the understanding of electronic processes at organic/perovskite heterojunctions present in planar PSC devices.

Author contributions

XG, LC and DCQ conceived the experiments. GJ, BZ, XZ and KS recorded the UPS and XPS spectra. YY collected the GIXRD and SEM data. GZ prepared the PSC device and characterized the performance. FS and YX contributed to interpretations. JG, LC, and XYG drafted the manuscript. All authors contributed to manuscript development.

Acknowledgements

XG and LC are grateful for the financial support by the National Natural Science Foundation of China (Grant No. 11175239, 21503233 and 11574317). We thank the staff at beamline BL14B1 at SSRF for help.

References

1 A. Kojima, K. Teshima, Y. Shirai and T. Miyasaka, *J. Am. Chem. Soc.*, 2009, **131**, 6050–6051.
2 D. Bi, W. Tress, M. I. Dar, P. Gao, J. Luo, C. Renevier, K. Schenk, A. Abate, F. Giordano, J.-P. C. Baena, J.-D. Decoppet, S. M. Zakeeruddin, M. K. Nazeeruddin, M. Grätzel and A. Hagfeldt, *Sci. Adv.*, 2016, **2**, e1501170.
3 M. Saliba, T. Matsui, J.-Y. Seo, K. Domanski, J.-P. Correa-Baena, M. K. Nazeeruddin, S. M. Zakeeruddin, W. Tress, A. Abate, A. Hagfeldt and M. Grätzel, *Energy Environ. Sci.*, 2016, **9**, 1989–1997.
4 S. D. Stranks, G. E. Eperon, G. Grancini, C. Menelaou, M. J. P. Alcocer, T. Leijtens, L. M. Herz, A. Petrozza and H. J. Snaith, *Science*, 2013, **342**, 341–344.
5 Q. Dong, Y. Fang, Y. Shao, P. Mulligan, J. Qiu, L. Cao and J. Huang, *Science*, 2015, **347**, 967–970.
6 D. Shi, V. Adinolfi, R. Comin, M. Yuan, E. Alarousu, A. Buin, Y. Chen, S. Hoogland, A. Rothenberger, K. Katsiev,

Y. Losovyj, X. Zhang, P. A. Dowben, O. F. Mohammed, E. H. Sargent and O. M. Bakr, *Science*, 2015, **347**, 519–522.
7 C. Motta, F. El-Mellouhi and S. Sanvito, *Sci. Rep.*, 2015, **5**, 12746.
8 H. S. Jung and N.-G. Park, *Small*, 2014, **11**, 10–25.
9 W. Chen, D.-C. Qi, H. Huang, X. Gao and A. T. S. Wee, *Adv. Funct. Mater.*, 2011, **21**, 410–424.
10 W. S. Yang, J. H. Noh, N. J. Jeon, Y. C. Kim, S. Ryu, J. Seo and S. I. Seok, *Science*, 2015, **348**, 1234–1237.
11 H. Zhou, Q. Chen, G. Li, S. Luo, T. Song, H.-S. Duan, Z. Hong, J. You, Y. Liu and Y. Yang, *Science*, 2014, **345**, 542–546.
12 N. Ahn, D.-Y. Son, I.-H. Jang, S. M. Kang, M. Choi and N.-G. Park, *J. Am. Chem. Soc.*, 2015, **137**, 8696–8699.
13 M. Saliba, S. Orlandi, T. Matsui, S. Aghazada, M. Cavazzini, J.-P. Correa-Baena, P. Gao, R. Scopelliti, E. Mosconi, K.-H. Dahmen, F. De Angelis, A. Abate, A. Hagfeldt, G. Pozzi, M. Graetzel and M. K. Nazeeruddin, *Nat. Energy*, 2016, **1**, 15017.
14 P. Ganesan, K. Fu, P. Gao, I. Raabe, K. Schenk, R. Scopelliti, J. Luo, L. H. Wong, M. Grätzel and M. K. Nazeeruddin, *Energy Environ. Sci.*, 2015, **8**, 1986–1991.
15 Z. Yu and L. Sun, *Adv. Energy Mater.*, 2015, **5**, 1500213.
16 Q.-K. Wang, R.-B. Wang, P.-F. Shen, C. Li, Y.-Q. Li, L.-J. Liu, S. Duhm and J.-X. Tang, *Adv. Mater. Interfaces*, 2015, **2**, 1400528.
17 P. Schulz, E. Edri, S. Kirmayer, G. Hodes, D. Cahen and A. Kahn, *Energy Environ. Sci.*, 2014, **7**, 1377–1381.
18 Y. Song, S. Lv, X. Liu, X. Li, S. Wang, H. Wei, D. Li, Y. Xiao and Q. Meng, *Chem. Commun.*, 2014, **50**, 15239–15242.
19 S. Kazim, F. J. Ramos, P. Gao, M. K. Nazeeruddin, M. Grätzel and S. Ahmad, *Energy Environ. Sci.*, 2015, **8**, 1816–1823.
20 S. F. Voelker, S. Collavini and J. Luis Delgado, *ChemSusChem*, 2015, **8**, 3012–3028.
21 H. A. Abbas, R. Kottokkaran, B. Ganapathy, M. Samiee, L. Zhang, A. Kitahara, M. Noack and V. L. Dalal, *APL Mater.*, 2015, **3**, 16105.
22 Q. Zhu, X. Bao, J. Yu, D. Zhu, M. Qiu, R. Yang and L. Dong, *ACS Appl. Mater. Interfaces*, 2016, **8**, 2652–2657.
23 A. S. Subbiah, A. Halder, S. Ghosh, N. Mahuli, G. Hodes and S. K. Sarkar, *J. Phys. Chem. Lett.*, 2014, **5**, 1748–1753.
24 K. Zhang, L. Wang, Y. Liang, S. Yang, J. Liang, F. Cheng and J. Chen, *Synth. Met.*, 2012, **162**, 490–496.
25 J. H. Noh, N. J. Jeon, Y. C. Choi, M. K. Nazeeruddin, M. Grätzel and S. I. Seok, *J. Mater. Chem. A*, 2013, **1**, 11842.
26 M. J. Currie, J. K. Mapel, T. D. Heidel, S. Goffri and M. A. Baldo, *Science*, 2008, **321**, 226–228.
27 Z. Zhi-lin, J. Xue-yin, X. Shao-hong, T. Nagatomo and O. Omoto, *J. Phys. D: Appl. Phys.*, 1998, **31**, 32.
28 M.-Y. Chang, Y.-K. Han, C.-C. Wang, S.-C. Lin, Y.-J. Tsai and W.-Y. Huang, *J. Electrochem. Soc.*, 2008, **155**, J365.
29 V. Podzorov, V. M. Pudalov and M. E. Gershenson, *Appl. Phys. Lett.*, 2003, **82**, 1739–1741.
30 A. Gaur and P. Kumar, *Appl. Phys. A: Mater. Sci. Process.*, 2012, **111**, 877–886.
31 N. Sato, K. Seki and H. Inokuchi, *J. Chem. Soc., Faraday Trans. 2*, 1981, **77**, 1621–1633.
32 J. Emara, T. Schnier, N. Pourdavoud, T. Riedl, K. Meerholz and S. Olthof, *Adv. Mater.*, 2016, **28**, 553–559.
33 S. Zhong, J. Q. Zhong, H. Y. Mao, J. L. Zhang, J. D. Lin and W. Chen, *Phys. Chem. Chem. Phys.*, 2012, **14**, 14127–14141.
34 H. Ishii, K. Sugiyama, E. Ito and K. Seki, *Adv. Mater.*, 1999, **11**, 605–625.
35 S. Braun, W. R. Salaneck and M. Fahlman, *Adv. Mater.*, 2009, **21**, 1450–1472.
36 L. Cao, Y. Wang, J. Zhong, Y. Han, W. Zhang, X. Yu, F. Xu, D.-C. Qi and A. T. S. Wee, *J. Phys. Chem. C*, 2011, **115**, 24880–24887.
37 P. Amsalem, J. Niederhausen, J. Frisch, A. Wilke, B. Bröker, A. Vollmer, R. Rieger, K. Müllen, J. P. Rabe and N. Koch, *J. Phys. Chem. C*, 2011, **115**, 17503–17507.
38 Z.-K. Wang, M. Li, Y.-G. Yang, Y. Hu, H. Ma, X.-Y. Gao and L.-S. Liao, *Adv. Mater.*, 2016, 1.
39 G. E. Eperon, V. M. Burlakov, P. Docampo, A. Goriely and H. J. Snaith, *Adv. Funct. Mater.*, 2014, **24**, 151–157.
40 J.-H. Im, H.-S. Kim and N.-G. Park, *APL Mater.*, 2014, **2**, 81510.
41 Q. Wang, Y. Shao, H. Xie, L. Lyu, X. Liu, Y. Gao and J. Huang, *Appl. Phys. Lett.*, 2014, **105**, 163508.
42 H. Xie, X. Liu, L. Lyu, D. Niu, Q. Wang, J. Huang and Y. Gao, *J. Phys. Chem. C*, 2016, **120**, 215–220.
43 L. K. Ono and Y. Qi, *J. Phys. Chem. Lett.*, 2016, **7**, 4764–4794.
44 Y. Jiang, E. J. Juarez-Perez, Q. Ge, S. Wang, M. R. Leyden, L. K. Ono, S. R. Raga, J. Hu and Y. Qi, *Mater. Horiz.*, 2016, **3**, 548–555.
45 G. E. Eperon, S. D. Stranks, C. Menelaou, M. B. Johnston, L. M. Herz and H. J. Snaith, *Energy Environ. Sci.*, 2014, **7**, 982–988.
46 N. Pellet, P. Gao, G. Gregori, T.-Y. Yang, M. K. Nazeeruddin, J. Maier and M. Grätzel, *Angew. Chem., Int. Ed.*, 2014, **53**, 3151–3157.
47 F. Hao, C. C. Stoumpos, R. P. H. Chang and M. G. Kanatzidis, *J. Am. Chem. Soc.*, 2014, **136**, 8094–8099.
48 C. Li, J. Wei, M. Sato, H. Koike, Z.-Z. Xie, Y.-Q. Li, K. Kanai, S. Kera, N. Ueno and J.-X. Tang, *ACS Appl. Mater. Interfaces*, 2016, **8**, 11526–11531.
49 J. Chang, H. Zhu, J. Xiao, F. H. Isikgor, Z. Lin, Y. Hao, K. Zeng, Q.-H. Xu and J. Ouyang, *J. Mater. Chem. A*, 2016, **4**, 7943–7949.
50 Z.-L. Tseng, C.-H. Chiang and C.-G. Wu, *Sci. Rep.*, 2015, **5**, 13211.
51 M. Shirayama, M. Kato, T. Miyadera, T. Sugita, T. Fujiseki, S. Hara, H. Kadowaki, D. Murata, M. Chikamatsu and H. Fujiwara, *J. Appl. Phys.*, 2016, **119**, 115501.
52 L. Huang, Z. Hu, G. Yue, J. Liu, X. Cui, J. Zhang and Y. Zhu, *Phys. Chem. Chem. Phys.*, 2015, **17**, 22015–22022.
53 X. Liu, C. Wang, L. Lyu, C. Wang, Z. Xiao, C. Bi, J. Huang and Y. Gao, *Phys. Chem. Chem. Phys.*, 2015, **17**, 896–902.
54 M. M. Lee, J. Teuscher, T. Miyasaka, T. N. Murakami and H. J. Snaith, *Science*, 2012, **338**, 643–647.
55 T. Ueba, J. Park, R. Terawaki, Y. Watanabe, T. Yamada and T. Munakata, *Surf. Sci.*, 2016, **649**, 7–13.
56 C. Wang, C. Wang, X. Liu, J. Kauppi, Y. Shao, Z. Xiao, C. Bi, J. Huang and Y. Gao, *Appl. Phys. Lett.*, 2015, **106**, 111603.

57 Y. Yamada, T. Nakamura, M. Endo, A. Wakamiya and Y. Kanemitsu, *Appl. Phys. Express*, 2014, **7**, 32302.
58 G. Ji, B. Zhao, F. Song, G. Zheng, X. Zhang, K. Shen, Y. Yang, S. Chen and X. Gao, *Appl. Surf. Sci.*, 2017, **393**, 417–421.
59 J. H. Seo, T. M. Pedersen, G. S. Chang, A. Moewes, K.-H. Yoo, S. J. Cho and C. N. Whang, *J. Phys. Chem. B*, 2007, **111**, 9513–9518.
60 B. Barış, H. G. Özdemir, N. Tuğluoğlu, S. Karadeniz, Ö. F. Yüksel and Z. Kişnişci, *J. Mater. Sci.: Mater. Electron.*, 2014, **25**, 3586–3593.
61 F. Bussolotti, S. Kera, K. Kudo, A. Kahn and N. Ueno, *Phys. Rev. Lett.*, 2013, **110**, 267602.
62 J. H. Heo, H. J. Han, D. Kim, T. K. Ahn and S. H. Im, *Energy Environ. Sci.*, 2015, **8**, 1602–1608.
63 L. M. Chen, Z. R. Hong, G. Li and Y. Yang, *Adv. Mater.*, 2009, **21**, 1434–1449.
64 J. W. Jo, M.-S. Seo, M. Park, J.-Y. Kim, J. S. Park, I. K. Han, H. Ahn, J. W. Jung, B.-H. Sohn, M. J. Ko and H. J. Son, *Adv. Funct. Mater.*, 2016, **26**, 4426.
65 N. Tuğluoğlu, B. Barış, H. Gürel, S. Karadeniz and Ö. F. Yüksel, *J. Alloys Compd.*, 2014, **582**, 696–702.
66 S. Bag and M. F. Durstock, *ACS Appl. Mater. Interfaces*, 2016, **8**, 5053–5057.